Quantum nanoconstrictions fabricated by cryo-etching in encapsulated graphene

V. Clericò,[†] J. A. Delgado-Notario,[†] M. Saiz-Bretín,[‡] A. V. Malyshev,[‡] Y. M. Meziani,[†] P. Hidalgo,[‡] B. Méndez,[‡] M. Amado,[†] F. Domínguez-Adame,[‡] and E. Diez[*,†]

[†]*Group of Nanotechnology, USAL-NANOLAB, Universidad de Salamanca, E-37008 Salamanca, Spain*

[‡]*Departamento de Física de Materiales, Universidad Complutense, E-28040 Madrid, Spain*

[*]E-mail: enrisa@usal.es

Phone: +34 670 581 543. Fax: +34 923 29 48 53

Abstract

More than a decade after the discovery of graphene, ballistic transport in nanostructures based on this intriguing material still represents a challenging field of research in two-dimensional electronics. The presence of rough edges in nanostructures based on this material prevents the appearance of truly ballistic electron transport as theoretically predicted and, therefore, not well-developed plateaus of conductance have been revealed to date. In this work we report on a novel implementation of the cryo-etching method, which enabled us to fabricate graphene nanoconstrictions encapsulated between hexagonal boron nitride thin films with unprecedented control of the structure edges. High quality smooth nanometer-rough edges are characterized by atomic force microscopy and a clear correlation between low roughness and the existence of well-developed quantized conductance steps with the concomitant occurrence of ballistic

transport is found at low temperature. In particular, we come upon exact $2e^2/h$ quantization steps of conductance at zero magnetic field due to size quantization, as it has been theoretically predicted for truly ballistic electron transport through graphene nanoconstrictions.

Keywords

Graphene nanoconstriction, cryo etching, quantized conductance

The use of two-dimensional (2D) materials for electronic-like devices blossomed after the discovery of graphene and represents an exciting whole field of research on its own. In such structures, the extreme existing aspect ratio, where the width W and length L of the devices exceed orders of magnitude the thickness, and the importance of manufacturing the devices with low-roughness borders, play a crucial role in the nature of the electronic transport. Graphene stands out as one of the most intriguing 2D materials in which the possibility of achieving a fully-tunable electronic confinement was pursued from its discovery.[1] In the ballistic regime, graphene is able to sustain quantized conductance with electron transport levels equally spaced in energy,[2] but not prior to overcome some issues such as the intrinsically moderate mobility in the single-layer-graphene samples and the importance of the borders in the mechanically exfoliated sheet of carbon atoms that can completely change the bulk conductance within the sample.[3] To overcome these problems that are detrimental for the study of pure ballistic transport, heterostructures of graphene encapsulated within thin layers of diverse 2D materials such as hexaboron-nitride (hBN)[4] have been manufactured, obtaining mobilities exceeding orders of magnitude those of the standalone single-layer-graphene structures. However, the problem of the roughness at the borders remains.

Single-layer and encapsulated-like graphene samples, where the width of the conductive layer has been narrowed down to few hundreds or eventually some tens of nanometers, have served as the template for the study of ballistic transport of carriers. To date, there have been two independent ways of achieving quantized conductance in graphene, either

using electrostatic potential gates placed on the top (underneath) the flake to confine the density of charge into a well defined area or by tailoring physically the two-dimensional flake into narrow structures, *i.e.* into nanoconstrictions (NCs), through a mechanical or chemical etching definition. While the first approach has shown a promising outcome with well defined conductance plateaus separated $2e^2/h$ and $4e^2/h$,[5,6] the latter has turned into an arduous technological challenge with no clear evidence of quantized plateaus. In the first mechanically-defined graphene NCs deposited directly onto silicon dioxide wafers,[1,7] the presence of a plethora of different transport effects such as Coulomb blockade, high electron backscattering and electron localization by disorder and charging effects, together with an intrinsically low mobility of carriers, resulted in conductance steps at least an order of magnitude lower than the conductance quantum $2e^2/h$.[8,9] Some years ago, Tombros *et al.*[10] observed $2e^2/h$ steps of conductance in a large mobility constriction on suspended graphene defined by current annealing. The nanostructure was build by passing a high current through a previously suspended graphene flake, stretching and deforming it into a NC-like structure. The main limitation of this method is purely technological since the accurate control of the dimensions of the graphene NC is unattainable.

As previously stated, the use of lattice-matched hBN layers was a great leap forward into high-quality nanostructures, allowing for the fabrication of much higher mobility devices with intercalated graphene.[11] Electron transport properties of samples of encapsulated graphene show signatures of quantum conductance in form of *kinks*.[12,13] Yet, the effect of roughness of the structure due to the intrinsic dielectric behavior of the hBN film and the lack of control in the edge-definition of the heterostructures (of paramount importance to reduce edge scattering) have been detrimental for the appearance of well-defined plateaus of conductance. The problem of edge-definition and high roughness values was partially overcome thanks to the definition of GNCs with exfoliated graphene on hydrophobic silicon oxide substrate with the use of hexamethyldisilazane (HMDS).[14,15] This method increases the graphene mobility for a fair period of time ($\sim$ 96 h) after its treatment. The results

presented in Refs. [14,15] shown quantized conductance at zero magnetic field that appears, once more, in form of *kinks*. This procedure represents a promising compromise between relatively high mobility and very good edge-definition (roughness of the order of 1 nm), but improvements on the etching definition in higher mobility and more stable graphene GNCs are most desirable.

In this work we present the fabrication method and characterization of NCs on encapsulated graphene where a cryo-etching technique commonly applied for bulk three-dimensional materials has been used in quasi-2D structures achieving an unprecedented control of the edge-definition. This technique was successfully implemented in silicon-based devices, where it was possible to control and define low-roughness sidewalls, observe the absence of sidewall scalloping,[16] and generate samples with a high aspect ratio and cleaning[17] in nanometric-size structures.[18] The extension of the cryo-etching technique to graphene allowed us to built NCs with very low sidewall roughness, as proved by atomic force microscopy (AFM) measurements. AFM micrographs were employed to assess the actual profile of the sample edges, that were later used as input in numerical simulations. We found an excellent agreement between the measured and calculated electrical conductivity and a good correspondence to the theoretical prediction as well.

We focus the attention on a hBN/graphene/hBN constriction of a few hundreds of nm width W. The fabrication process started from heterostructures of hBN/graphene/hBN, obtained by dry transfer technique in a way very similar to the one reported by Pizzocchero *et al.*[19] An area free of impurities and bubbles in the hBN was selected by inspecting the different heterostructures with an optical Raman confocal microscope ($\lambda = 532\,\text{nm}$, $600\,\text{g/mm}$ grating and spot size $1\,\mu\text{m}$, see supplemental material S1). A first electron beam lithography (EBL) and a dry etching process in induced coupled plasma with SF_6 atmosphere were subsequently performed to define a bar-like structure in the hBN/graphene/hBN heterostructure. A rapid thermal annealing in Ar atmosphere at 350 °C for 15 minutes removed eventual small non-visible bubbles. With a second self-aligned EBL step and the electron beam evaporation

of Cr/Au (5/45 nm) we defined and deposited side contacts for electric measurements.

The constrictions were defined by means of the innovative cryo-etching process in graphene-based structures in the third aligned EBL step, which was performed at $-110\,^{\circ}\mathrm{C}$ in a controlled Ar/SF_6 (10/40 sccm) atmosphere (see supplemental information S2). The use of a polymethylmethacrylate (PMMA) mask for this etching process represents a less invasive approach for encapsulated graphene-structures compared to the use of a Cr mask in submicron-size constrictions.[12] To the best of our knowledge, this is the first time that a cryo-etching method is successfully used for the definition of graphene nanostructures.

Figure 1a shows a tilted SEM micrograph of a typical NC in encapsulated graphene defined by cryo-etching. The lateral width of this NC is $W \simeq 206\,\mathrm{nm}$ and the length is $L \simeq 200\,\mathrm{nm}$. The inset shows the SEM micrograph at higher magnification, in which the sandwiched structure (hBN/graphene/hBN) is colored in sky blue. A standard 4–probes configuration to perform the electronic characterization at low-temperatures is sketched in the figure, where a pseudo-dc (13 Hz) current of 5 nA was injected/collected from the outer contacts while the voltage drop was measured by an in-phase lock-in preamplifier closer to the constriction (the contacts are gold colored for better clarity). The result of a typical measurement at $T = 3.1\,\mathrm{K}$ is depicted in Figure 1b. The conductance in units of e^2/h is displayed as a function of the normalized back-gate voltage $\Delta V_g = V_g - V_g^*$, V_g^* being the value of the voltage at the Dirac point. The conductance is directly obtained by the measured contactless resistance as $G = 1/R$. In our sample the hole-side region ($\Delta V_g < 0$) is always better resolved than the electron one ($\Delta V_g > 0$), where the ballistic behaviour starts at higher back-gate voltage due to the residual charge density. For this reason, in the main text we restrict our discussion to the hole-side (see supplementary information S4 for the electron-side regime). The typical mobility in our devices is $\mu \simeq 150\,000\,\mathrm{cm}^2/\mathrm{Vs}$ at room temperature, as shown in the supplementary information S3, obtained by means of the field effect formula.[20]

The quality of the graphene NCs is apparent in the SEM micrograph shown in Figure 1a.

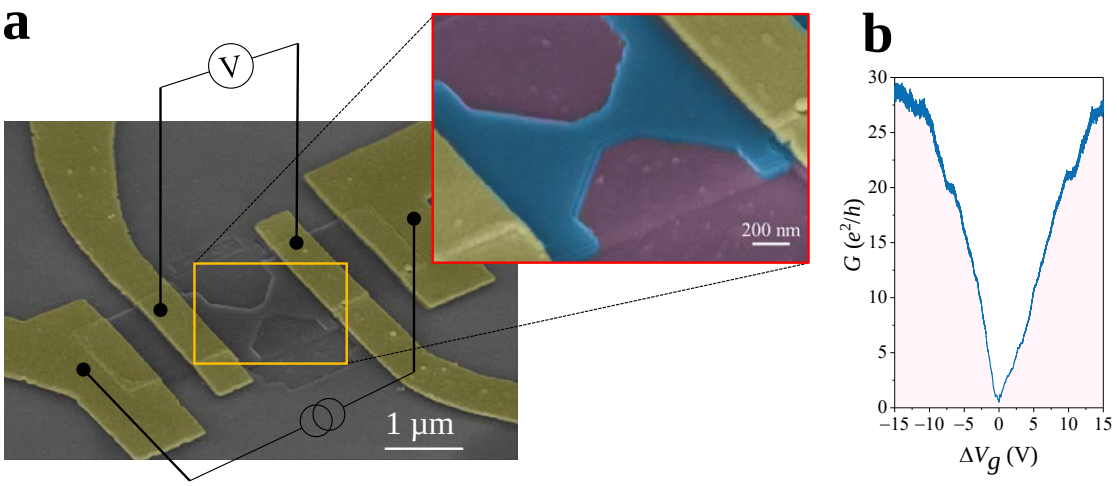

Figure 1: (a) Tilted SEM micrograph of an encapsulated graphene NC with lateral width $W \simeq 206\,\text{nm}$ and length $L \simeq 200\,\text{nm}$ including an schematic view of the electronic setup. The inset shows an enlarged view where the hBN/graphene/hBN heterostructure is colored in sky blue, the SiO_2 substrate (partially etched) in violet and the contacts in yellow gold. (b) Conductance as a function of the normalized voltage $\Delta V_g = V_g - V_g^*$ for the same NC measured at $T = 3.1\,\text{K}$.

However, in order to get a quantitative analysis of the edge roughness, AFM measurements were performed in our samples. We have used a Nanotech AFM instrument operating in contact mode. Figure 2a displays the AFM image of the whole NC. The edge and the corresponding contour profile within the square marked in panel (a) are shown in Figure 2b. The AFM images reveal the excellent definition of our graphene NC and, in particular, the smooth sidewall. The contour plot (black line in Figure 2b) is taken 15 nm under the top hBN flake (with a thickness of about 15 nm) in order to assess the actual size and roughness of the NC. The average edge roughness can be estimated by zooming in this profile and then a roughness around 2 nm is obtained (see Figure 2c). This value is not far from the edge roughness estimated in lower mobility graphene NCs on HMDS,[14] namely without hBN, where the value was of the order of 1 nm. Our measurement represents the first quantitative estimation of the roughness observed in encapsulated graphene nanoconstrictions as well.

Thanks to the accurate profile obtained with AFM measurements, we are able to study also the real edge roughness in our simulations based on a tight binding model. The electronic

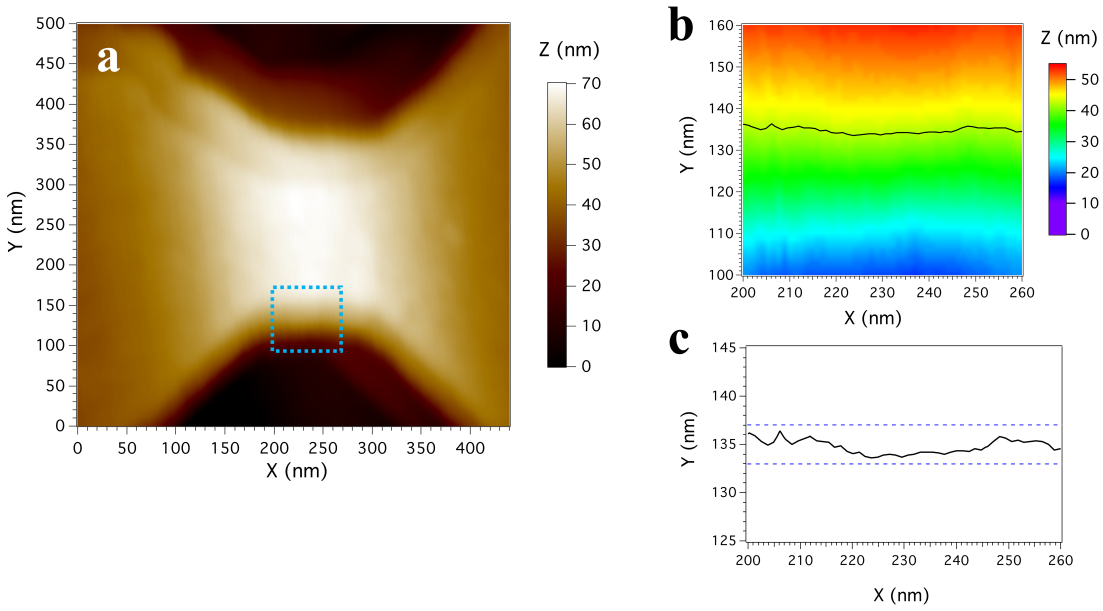

Figure 2: (a) AFM image of the graphene NC with $W = 206\,\text{nm}$. (b) Contour plot taken from the square highlighted in panel (a), at 15 nm from the top of the nanostructure. (c) Enlarged view of the contour plot, where the dashed lines indicate the values used to estimate the edge roughness.

properties of graphene close to Dirac point can be accurately described by a tight-binding Hamiltonian for π electrons, $\mathcal{H} = -\sum_{\langle i,j\rangle} t_{ij}|i\rangle\langle j|$, where $|i\rangle$ is the atomic orbital of the i-th carbon atom.[21] The corresponding orbital energy level is set as the origin of energy without losing generality. Here t_{ij} stands for the hopping energy parameter between orbitals of the i-th and j-th carbon atoms and has been set to be constant between nearest-neighbor atoms ($t_{ij} = 2.8\,\text{eV}$, see Ref. [22]) and zero otherwise. Such approximation provides reliable results near the K and K' points of the Brillouin zone, as already reported in Ref. [23].

Neglecting electron-phonon[24,25] and electron-electron[26] interactions in our calculations, we consider electrons in the fully coherent regime, hence with ballistic motion through the whole device. Combining the *quantum transmitting boundary method*, based on a finite element approximation,[27] and an *effective transfer matrix method* adapted for graphene (see Ref. [28] for technical details), the wave function in the whole sample and the transmission coefficient $\tau_n(E)$ for each mode at an energy E is calculated. These modes, also known as channels or subbands, arise from the transverse quantization due to the lateral confinement

at the leads.[29] According to the Buttiker-Landauer formalism,[29] at very low temperature the electrical conductance is proportional to the transmission coefficient at the Fermi energy E_F

$$G = \frac{2e^2}{h} \sum_n \tau_n(E_F) \ , \tag{1}$$

where the index n runs over the transverse modes. The factor 2 accounts the spin degeneracy whereas the valleys are considered explicitly in our tight-binding calculation of the transmission coefficient τ_n. As the NC becomes wider, the number of transverse modes for a given energy increases and so does the conductance. But interestingly, we found that the main features are essentially the same provided that the conductance is plotted against Wk_F, where k_F is the Fermi wavenumber and W is the NC width. This has an important practical consequence, namely we can extrapolate results to much larger systems as the ones fabricated experimentally and otherwise computationally very expensive (or even impossible) to simulate.

In the low-temperature regime, when the elastic mean free path l_m is larger than the GNC length $L = 206\,\text{nm}$, transport is ballistic. We have estimated from the carrier mobility of our GNC that $l_m > 1\,\mu\text{m}$ (see supplementary information S3) in the temperature range considered in this work. Hence conditions for ballistic transport are largely satisfied and therefore the conductance should be also described by the commonly used Sharwin formula[12,30–32] (replacing the usual factor 2 by a factor 4 to account for both spin and valley degeneracies in graphene) showing a linear dependence of Wk_F

$$G = \frac{4e^2}{\pi h} Wk_F t \ , \tag{2}$$

where t is the transmission parameter, being $t = 1$ for the ideal ballistic transport.

Figure 3a shows the conductance G as a function of Wk_F measured at $T = 3.1\,\text{K}$ (red line) and the theoretical conductance (blue line) from our tight-binding simulations with the same edge roughness obtained from the AFM measurements (Figure 2).

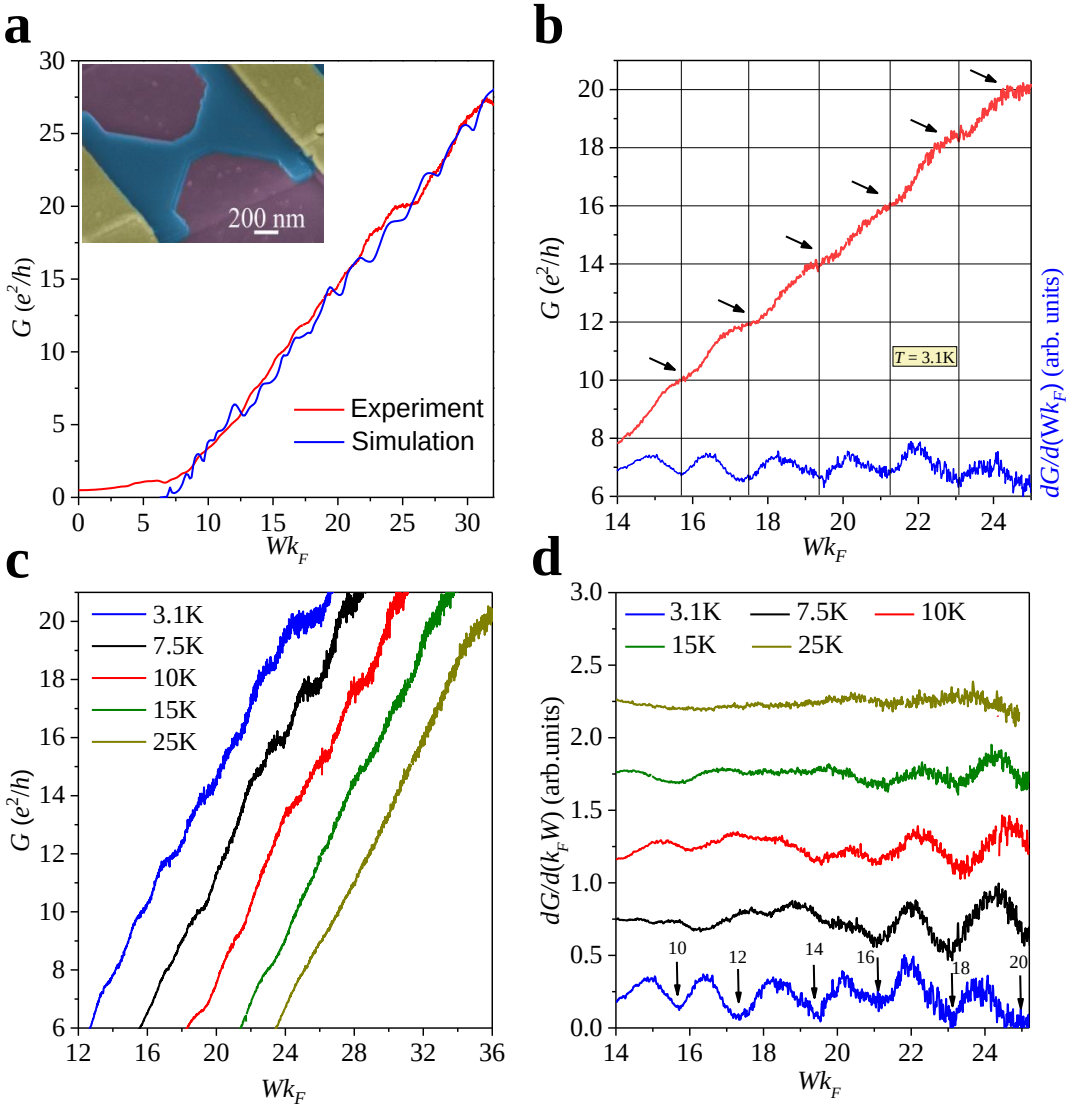

Figure 3: (a) Comparison of simulated and experimental conductance of a GNC of width $W = 206\,\text{nm}$. (b) Conductance (red line) and transconductance (blue line) as a function Wk_F measured at $T = 3.1\,\text{K}$. Solid black arrows show the position of the plateaus of conductance separated by $2e^2/h$ and matching integer values from $G = 10e^2/h$ onwards. (c) Evolution of G as a function of Wk_F at different temperatures. The curves have been horizontally shifted by a factor $2.5Wk_F$ for clarity. (d) Temperature dependence of the transconductance as a function of Wk_F. Black solid arrows represent the value of the plateaus of conductance in units of e^2/h at $T = 3.1\,\text{K}$, matching the position of the minima in $dG/d(Wk_F)$.

We note the good agreement of the experimental and simulated conductance as well as the linear dependence on Wk_F, characteristic of ballistic transport above a threshold value Wk_F^0.

From the normalized gate voltage ΔV_g we can obtain the carrier density n and therefore the Fermi wavenumber $k_F = \sqrt{\pi n}$. Due to the presence of residual doping in our NC, we cannot tune the carrier density below a minimum value $n_0 \sim 3.3 \times 10^{10}\,\mathrm{cm}^{-2}$ experimentally, and accordingly Wk_F could not be tune below a threshold value $Wk_F^0 = \sqrt{\pi n_0}\,W \sim 6.7$. The transmission parameter t is estimated from the linear fit of the conductance when $Wk_F > Wk_F^0$ using Equation (2). It is worth stressing the remarkable agreement of the slopes obtained from the theoretical and experimental conductance curves, yielding the transmission parameter $t = 0.9$. This value is close to the fully transmitted carrier regime $t = 1$, in contrast to the $t \sim 0.6$ given in Ref. [12] for a graphene NC with a comparable width of $W = 230\,\mathrm{nm}$ that was not defined by cryo-etching. For the electron-side ($V_g > V_g^*$), we also found a very similar transmission parameter $t = 0.9$, as presented in the supplemental information S4. This result, supported by the remarkable agreement with theoretical calculations using realistic profiles of the edge roughness, is a clear indication of ballistic transport due to the very high mobility and smooth edges that arise from the novel use of the cryo-etching procedure in their preparation. The estimated value of t in our structure is also significantly higher than the one obtained in much narrower NCs of width $W = 100\,\mathrm{nm}$ produced by means of a HMDS treatment.[14,15] In these samples, low-roughness edges are generated mainly due to the fact that the etching process on a single layer graphene is more controllable and a clean edge on a single layer of material is easier to attain than the one obtained on a thicker encapsulated graphene nanostructure. The study of graphene NCs obtained by means of a HMDS treatment is also presented in the supplementary information for comparison (S5 and S6). In that case, the corresponding transmission parameters are significantly lower than the ones found in encapsulated graphene NCs defined by cryo-etching.

A closer inspection of the conductance G (red line) and the dimensionless transconductance $dG/d(Wk_F)$ (blue line) versus Wk_F is shown in Figure 3b, signaling the second goal of this work. The plateaus of quantized conductance are clearly observed at regular intervals of Wk_F, corresponding to equally spaced marked minima of the transconductance.

The quantization of G is also very clear after reverting the direction of the current (see supplemental material S4). Up to six plateaus appear at values of the conductance of $G = 10,\ 12,\ 14,\ 16,\ 18,\ 20\,e^2/h$, hence the jump between neighbouring plateaus has been found to be $2e^2/h$. This value matches the theoretical estimation by Guimarães *et al.*, where the conductance of a graphene NC where $W \sim L$ is quantized into well-defined plateaus separated by $2e^2/h$.[33] Ihnatsenka *et al.* put forward electron-electron interaction and boundary scattering as the major responsible for the appearance of plateaus separated by $2e^2/h$ instead of $4e^2/h$,[34] as it would be expected in ideal nanoribbons with perfectly smooth edges where both spin and valley degeneracy are preserved.[5] To the best of our knowledge, this is the largest number of plateaus of conductance observed in single layer graphene samples that have been have been physically narrowed down into nanoconstriction-shape to date. While in bilayer graphene it is noticeably easier to confine carriers due to the presence of an already existing gap and hence plateaus of conductance are easier to achieve,[6,35] shaping electrostratically the conductive region into a constriction[5,6] allows to narrow-down the constriction further into a few tens of nm wide structure and to diminish the number of channels responsible of electric conduction. Our approach becomes a good compromise to achieve almost fully transmitted structures with smooth sidewalls where a systematic experimental study of NCs having differing widths may developed. In Figure 3c we present the temperature dependence of the conductance (taken at $T = 3.1,\ 7.5,\ 10,\ 15$ and 25K), where the curves have been shifted by a factor of $2.5Wk_F$ for clarity. The presence of the plateaus is clear and they are noticeably visible below $T \sim 10\,\mathrm{K}$. They start to smear out at higher temperatures until they are completely washed out at $T = 25\,\mathrm{K}$. Such a temperature dependence of G can be better studied by inspecting the dimensionless transconductance as presented in Figure 3d. The amplitude of the periodic oscillations of the transconductance as a function of Wk_F decreases by increasing temperature and finally disappear above $T = 15\,\mathrm{K}$. A similar threshold temperature for the vanishing of the conductance quantization was very recently found in bilayer graphene constrictions.[35] This behavior differs markedly from other

non-desired effects, such as localized charge carriers, that disappear at higher temperature (see supplemental information S8).

In summary, we have proposed a novel implementation of the cryo-etching method, which we used for fabrication of high quality graphene nanoconstrictions. The main advantage of the method is an unprecedented control of the edge definition and reduced roughness. The latter enabled us to fabricate high-mobility hBN-encapsulated graphene nanoconstrictions with well defined, sharp and extraordinarily smooth edges. These systems have been characterised by the standard AFM imaging techniques and then the obtained data on the realistic geometry was used in the large scale theoretical transport calculations. Results of such modelling agree very well with our experimental measurements and suggest that the transport in the system is almost fully ballistic. In particular, both the predicted and measured values of the transmission parameter are as high as $t = 0.9$. On the other hand, the size quantization is clearly manifesting itself as a ladder of several equally $2e^2/h$-spaced plateaus of conductance at temperatures up to $T = 10$ K, confirming the high quality of the samples. We claim that the cryo-etching technique paves to study truly-ballistic-high-mobility graphene-based nanostructures where definition of the edges and the control of the scattering processes are crucial.

Acknowledgement

This research has been supported by the Agencia Estatal de Investigación of Spain (Grants MAT2015-65274-R, MAT2016-75955 and TEC2015-65477-R), and the Junta de Castilla y León (Grant SA256P18), including FEDER funds from the European Commission. V. C. acknowledges N. Tombros and P. J. Zomer for introducing him in the transfer technique of two-dimensional materials. We are also thankful to D. López and M. Velázquez for their kind help with Raman measurements.

References

(1) Han, M. Y.; Özyilmaz, B.; Zhang, Y.; Kim, P. *Phys. Rev. Lett* **2007**, *98 29*, 206805.

(2) van Wees, B. J.; van Houten, H.; Beenakker, C. W. J.; Williamson, J. G.; Kouwenhoven, L. P.; van der Marel, D.; Foxon, C. T. *Phys. Rev. Lett* **1988**, *60*, 848.

(3) Caridad, J. M.; Calogero, G.; Pedrinazzi, P.; Santos, J. E.; Impellizzeri, A.; Gunst, T.; Booth, T. J.; Sordan,; Bøggild, P.; Brandbyge, M. *Nano Lett.* **2018**, *8*, 4675.

(4) Kretinin, A. V. et al. *Nano Lett.* **2014**, *14*, 3270.

(5) Kim, M.; Choi, J.-H.; Lee, S.-H.; Watanabe, K.; Taniguchi, T.; Jhi, S.-H.; Lee, H.-J. *Nat. Phys.* **2016**, *12*, 1022.

(6) Overweg, H.; Eggimann, H.; Chen, X.; Slizovskiy, S.; Eich, M.; Pisoni, R.; Lee, Y.; Rickhaus, P.; Watanabe, K.; Taniguchi, T.; Fal'ko, V.; Ihn, T.; Ensslin, K. *Nano Lett.* **2018**, *18*, 553.

(7) Lu, Y.; Goldsmith, B.; Strachan, D.; Lim, J. H.; Luo, Z.; Charlie Johnson, A. T. *Small* **2010**, *6*, 2748.

(8) Lin, Y.-M.; Perebeinos, V.; Chen, Z.; Avouris, P. *Phys. Rev. B* **2008**, *78*, 161409(R).

(9) Lian, C.; Tahy, K.; Fang, T.; Li, G.; Xing, H. G.; Jena, D. *Appl. Phys. Lett.* **2010**, *96*, 103109.

(10) Tombros, N.; Veligura, A.; Junesch, J.; Guimarães, M. H. D.; Vera-Marun, I. J.; T., J. H.; van Wees, B. *Nat. Phys.* **2011**, *7*, 697.

(11) Bischoff, D.; Varlet, A.; Simonet, P.; Eich, M.; Overweg, H. C.; Ihn, T.; Ensslin, K. *Appl. Phys. Rev.* **2015**, *2*, 031301.

(12) Terrés, B.; Chizova, L. A.; Libisch, F.; Peiro, J.; Jörger, D.; Engels, S.; Girschik, A.; Watanabe, K.; Taniguchi, T.; Rotkin, S. V.; Burgdörfer, J.; Stampfer, C. *Nat. Commun.* **2016**, *7*, 11528.

(13) Somanchi, S.; Terrés, B.; Peiro, J.; Staggenborg, M.; Watanabe, K.; Taniguchi, T.; Beschoten, B.; Stampfer, C. *Ann. Phys. (Berlin)* **2017**, *529*, 1700082.

(14) Caridad, J. M.; Power, S. R.; Lotz, M. R.; Shylau, A. A.; Thomsen, J. D.; Gammelgaard, L.; Booth, T. J.; Jauho, A.-P.; Bøggild, P. *Nat. Commun.* **2018**, *9*, 659.

(15) Clericò, V.; Delgado Notario, J. A.; Saiz-Bretín, M.; Hernández Fuentevilla, C.; Malyshev, A. V.; Lejarreta, J. D.; Diez, E.; Domínguez-Adame, F. *Phys. Status Solidi A* **2018**, *215*, 1701065.

(16) Defforgea, T.; Songa, X.; Gautiera, G.; Tillocherc, T.; Dussartc, R.; Sébastien Kouassi, S.; Tran-Van, F. *Sens. Actuators A Phys.* **2011**, *170*, 114.

(17) Cadarso, V. J.; Chidambaram, N.; Jacot-Descombes, L.; Schift, H. *Microsyst. Nanoeng.* **2017**, *3*, 17017.

(18) Liu, Z.; Wu, Y.; Harteneck, B.; Olynick, D. *Nanotechnology* **2013**, *24*, 015305.

(19) Pizzocchero, F.; Gammelgaard, L.; Jessen, B. S.; Caridad, J. M.; Wang, L.; Hone, J.; Bøggild, P.; Booth, T. J. *Nat. Comm.* **2016**, *7*, 11894.

(20) Kim, S.; Nah, J.; Jo, I.; Shahrjerdi, D.; Colombo, L.; Yao, Z.; Tutuc, E.; Banerjee, S. K. *Appl. Phys. Lett.* **2009**, *94*, 062107.

(21) Wallace, P. R. *Phys. Rev.* **1947**, *71*, 622.

(22) Castro Neto, A. H.; Guinea, F.; Peres, N. M.; Novoselov, K. S.; Geim, A. K. *Rev. Mod. Phys.* **2009**, *81*, 109.

(23) Reich, S.; Maultzsch,; Thomsen, C. *Physical Review B* **2002**, *66*, 035412.

(24) Morozov, S. V.; Novoselov, K. S.; Katsnelson, M. I.; Schedin, F.; Elias, D. C.; Jaszczak, J. A.; Geim, A. K. *Phys. Rev. Lett.* **2008**, *100*, 016602.

(25) Milošević, I.; Kepčija, N.; Dobardžić, E.; Damnjanović, M.; Mohr, M.; Maultzsch, J.; Thomsen, C. *Int. J. Mod. Phys. B* **2010**, *24*, 655.

(26) Li, X.; Barry, E. A.; Zavada, J. M.; Nardelli, M. B.; Kim, K. W. *Appl. Phys. Lett.* **2010**, *97*, 082101.

(27) Lent, C. S.; Kirkner, D. J. *J. Appl. Phys.* **1990**, *67*, 6353.

(28) Munárriz, J. *Modelling of plasmonic and graphene nanodevices*; Springer: Berlin, 2014.

(29) Datta, S. *Electronic transport in mesoscopic systems*; Cambridge University Press: Cambridge, 1995.

(30) Sharwin, Y. V. *Sov. Phys. JETP* **1965**, *21*, 655.

(31) de Jong, M. J. M. *Phys. Rev. B* **1994**, *49*, 7778.

(32) Kumar, K. et al. *Nature Physics* **2017**, *13*, 1182.

(33) Guimarães, M. H. D.; Svevtsov, O.; Waintal, X.; van Wees, B. J. *Phys. Rev. B* **2012**, *85*, 075424.

(34) Ihnatsenka, S.; ; Kirczenow, G. *Phys. Rev. B* **2012**, *85*, 121407(R).

(35) Lee, H.; Park, G.-H.; Park, J.; Lee, G.-H.; Watanabe, K.; Taniguchi, T.; Lee, H. *Nano Lett.* **2018**, *18*, 5961.

Quantum nanoconstrictions fabricated by cryo-etching in encapsulated graphene

V. Cleric`o,[†] J. A. Delgado-Notario,[†] M. Saiz-Bret´ın,[‡] A. V. Malyshev,[‡] Y. M. Meziani,[†] P. Hidalgo,[‡] B. M´endez,[‡] M. Amado,[†] F. Dom´ınguez-Adame,[‡] and E. Diez*,[†]

[†]*Group of Nanotechnology, USAL-NANOLAB, Universidad de Salamanca, E-37008 Salamanca, Spain*

[‡]*Departamento de Física de Materiales, Universidad Complutense, E-28040 Madrid, Spain*

E-mail: enrisa@usal.es

Phone: +34 670 581 543. Fax: +34 670 581 543

Nanoconstrictions in encapsulated graphene

S1. Raman spectra

The quality of hBN/graphene/hBN heterostructure is especially affected by the number of blister or bubbles of air, water or hydrocarbons trapped at the interfaces. they represent a contaminant for the heterostructures and for this reason it is necessary to exploit the area free of these blisters.[1] After a first qualitatively assessment with optical microscope, we have chosen the best areas of the different heterostructures (free of bubbles) and performed micro-Raman spectroscopy measurements. Figure S1 shows the Raman spectrum of the final hBN/Graphene/hBN heterostructure on a SiO_2/Si substrate. An indication of high quality graphene is given by the ratio between the 2D-peak and the G-peak, for example for

graphene on SiO_2 this value can vary betweeen 1 (defected graphene) until 3-4,[2] in suspended graphene it is typically 10.[3] In our case this ratio is around 10 (see Figure S1), larger than the value observed in heterostructures obtained with similar methods.[4] Another indication of the high quality of the hBN/graphene/hBN heterostructure is given by the Full Width Half Maximum (FWHM) of the 2D peak, a reduction of its value represents an improvement in the quality of the graphene flake. We found a value close to $18.6\,cm^{-1}$, while in graphene flakes on Si/SiO_2 substrate is typically above $30\,cm^{-1}$ on SiO_2/Si due structural deformations that broaden the 2D band.[5]

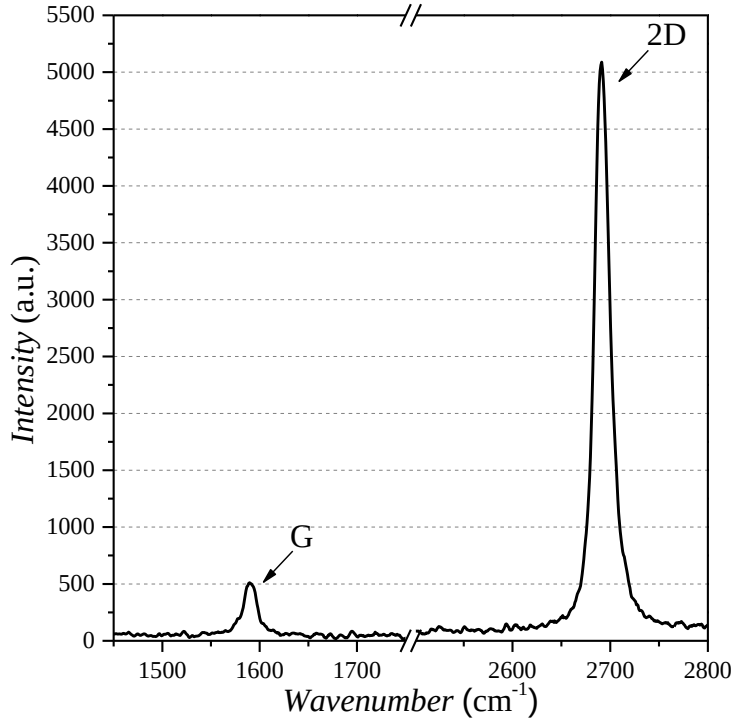

Figure S1: Typical Raman spectra of one of our hBN/graphene/hBN heterostructures.

S2. Cryo-etching process

In our fabrication process we introduced a cryo-etching step to define the graphene nanoconstriction. Cryogenic etch is in reality a technique introduced in 1980s, it was employed for the etching of the Silicon with high aspect ratios at cold temperatures. The main limitation is due to the necessity of liquid nitrogen, so an high cost of the cryo etch process. It had led the disuse of cryo etch and the develop of alternative etching technique, as the Bosch process.

We used for the first time a cryo-etching process to graphene devices. Our ICP-RIE (PlasmaPro 100 Cobra system) is, in fact, equipped with a cryogenic module, enabling to operate down to $-120\,^{\circ}\mathrm{C}$ to perform cryo-etching.

In Figure S2 the SEM images of a NCs etched on hBN with the cryo-etching technique (magnification of 450k) (a) and at room temperatures (magnification of 300k) (b). In the upper part there are the original SEM images in gray scale, in the lower part the coloured SEM images help the reader to visualize the borders. The higher roughness of the second image is evident in the edges, in comparison with the very well defined cryo-etched structure.

S3. Mobility and electron mean free path

In Figure S3a, the 4-probes resistance of encapsulated graphene versus the charge density is shown (before constriction definition) at room temperature. The carrier density n is related to the gate voltage V_g as follows

$$n = \frac{C_{\mathrm{ox}}}{e}\left(V_g - V_g^*\right) \ , \tag{1}$$

where C_{ox} is the capacitance per unit area and $V_g - V_g^*$ is the voltage with respect to the charge neutrality point and e the elementary charge.

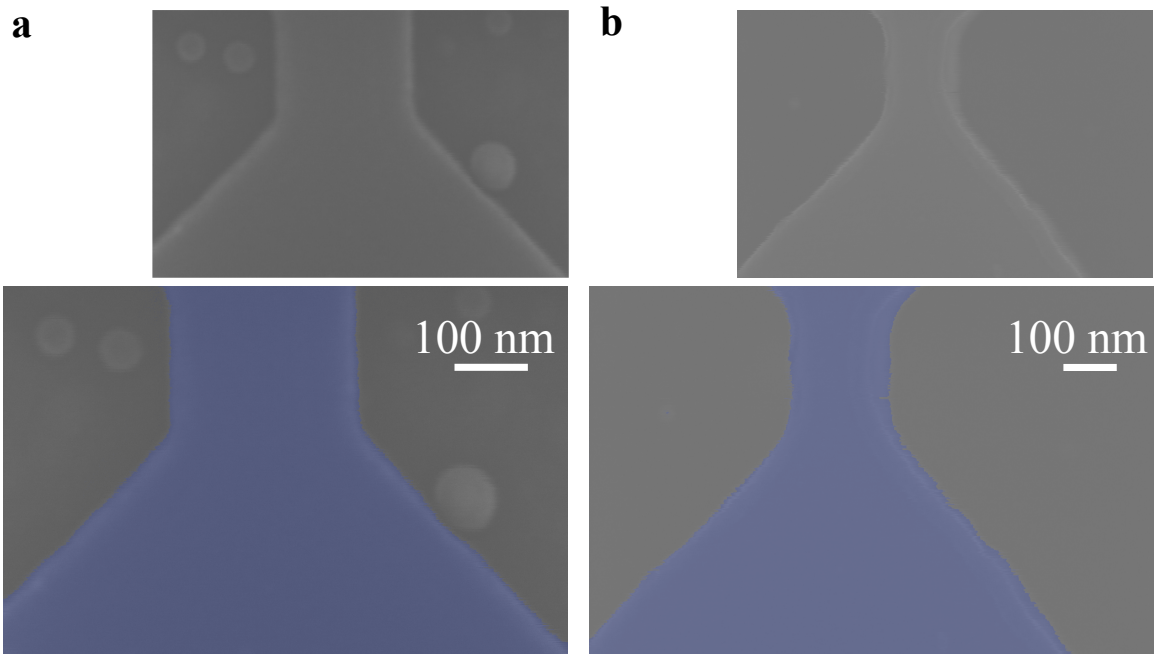

Figure S2: (a) SEM image of a NC etched with cryo-etching technique. Three bubbles appear in the image, they are blister of air trapped into the original heterostructures and in this case they are transferred to the substrate after the etching process (so they do not affect the device). (b) SEM image of a NC on hBN etched with simple ICP-RIE. The upper panel of each column shows the original SEM images in grey scale and the lower panels display the coloured ones.

According the Ref. [6], the relation of the resistance R and the mobility μ is given by

$$R = \frac{N_{\mathrm{sq}}}{e\mu\sqrt{n_0^2 + n^2}} \ , \tag{2}$$

where N_{sq} is the number of squares in a graphene channel, that is, the length over the width, μ is the mobility and n_0 is the residual doping. The estimated mobility is $142\,000\,\mathrm{cm}^2\,\mathrm{V}^{-1}\,\mathrm{s}^{-1}$ for holes (red dashed line) and $152\,000\,\mathrm{cm}^2\,\mathrm{V}^{-1}\,\mathrm{s}^{-1}$ for electrons (blue dashed line). From the mobility we can determine the elastic free mean path $l = \mu\hbar/e\sqrt{n\pi}$. For an electron density $n \approx 1 \times 10^{12}\,\mathrm{cm}^{-2}$ we obtain a value of l larger than $1.5\,\mu\mathrm{m}$, that is, the dimension of the distance between the probes. Therefore, we can confidently assume a truly ballistic regime in the whole nanostructure.

Figure S3(b) displays the conductance at room temperature as a function of the normal-

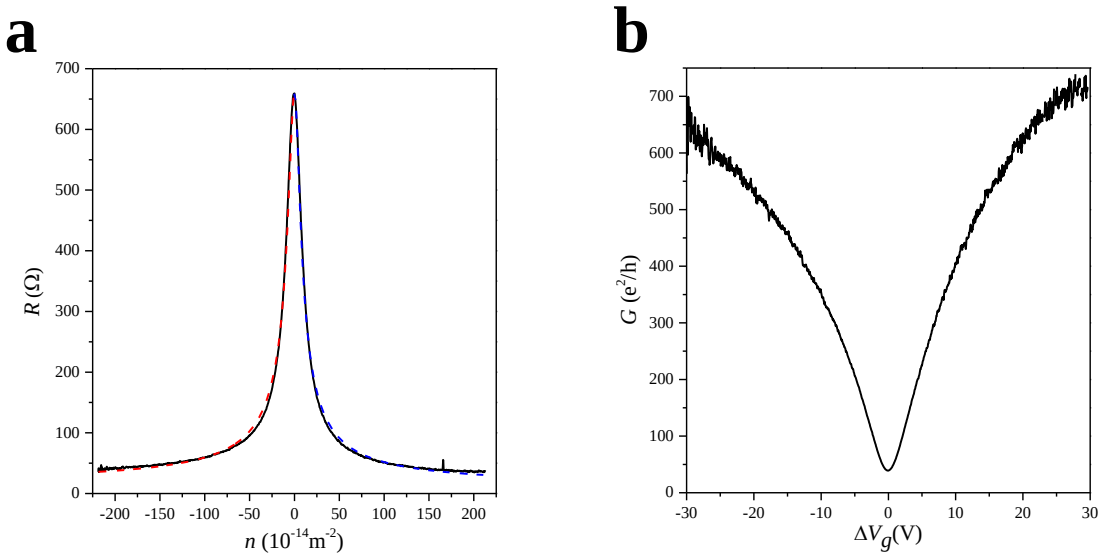

Figure S3: (a) 4-probes resistance of a graphene encapsulated device (before constriction definition) in function of the charge density n at room temperature. The mobility is estimated from Equation (2) for holes (red dashed line) and electron (blue dashed line). (b) From the resistance we can calculate the conductance as $G = 1/R$. G is plotted in units of e^2/h as a function of the gate voltage.

ized gate voltage. With the 4-probes configuration, the conductance is directly obtained from the resistance as $G = 1/R$. The high values of conductance observed in our encapsulated devices are a clear signature of a very high mobility regime.

S4. Transmission parameter of holes and electron side

In Figure S4a, the conductance of 206 nm encapsulated graphene as function of the Fermi wave number k_F for the hole side ($V_g - V_g^* < 0$) is shown. The quantization steps are clearly developed for forward and backward currents (black and red line). The small shift in the red line is due to the residual gate doping but it does not affect the slope (proportional to the transmission parameter t). A linear fit of the conductance as a function of Wk_F shown in Figures S4a and S4b leads to transmission parameters $t = 0.865$ and $t = 0.863$ for the hole and electron sides, respectively. These values are very close to each other. Furthermore, they are closer to unity than the value previously reported in Ref. [7]. It is also apparent

the larger residual carrier density in the electron side, yielding a threshold Fermi wavevector $k_F^0 \approx 65 \times 10^6\,\mathrm{m}^{-1}$.

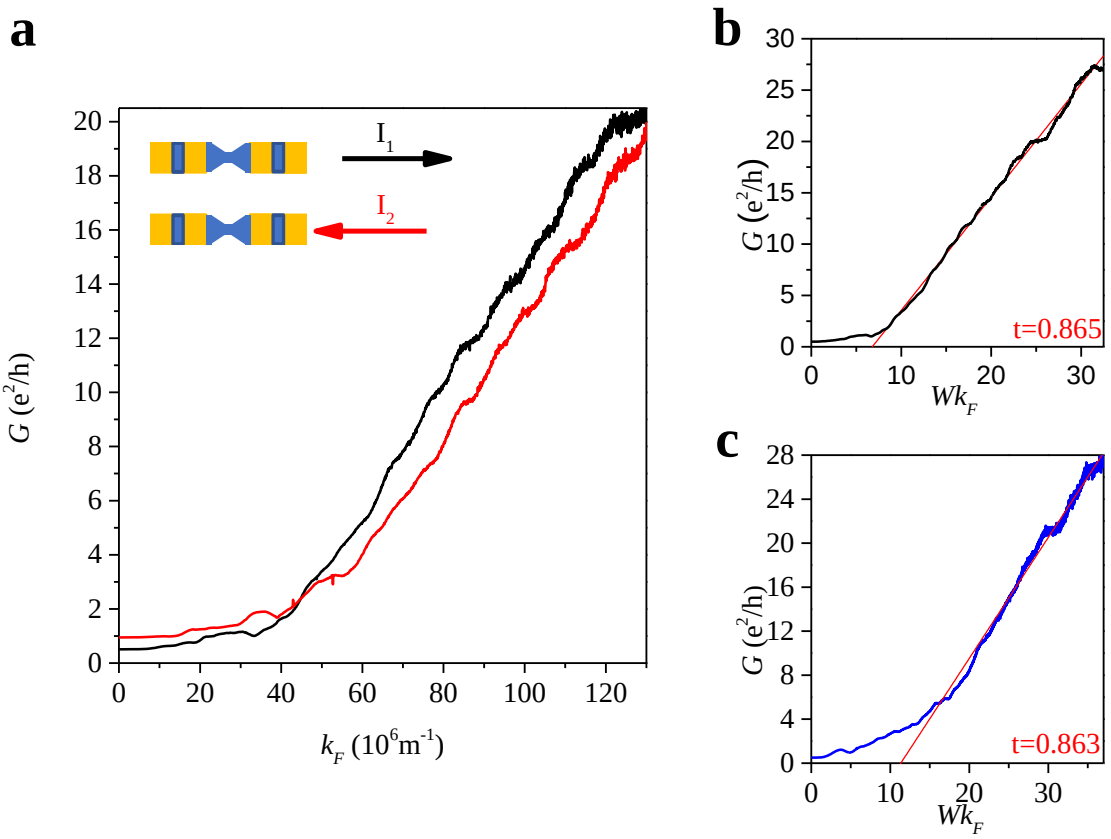

Figure S4: (a) Conductance in units of e^2/h versus the Fermi wavenumber k_F for forward and backward currents at the hole side, showing well-defined plateaus of the conductance. The transmission parameter t is obtained from the linear fitting of the conductance (in units of e^2/h) as a function of Wk_F for the (b) hole side ($t = 0.865$) and (c) electron side ($t = 0.863$). The width of the constriction is $W = 206\,\mathrm{nm}$.

Hexamethyldisilazane graphene nanoconstriction (GNC)

For graphene nanoconstrictions (GNC) and nanoribbons (GNR) produced with a hexamethyldisilazane (HMDS) treatment, a clean piece of $1\,\mathrm{cm}^2$ Si/SiO_2 substrate was dipped in a $1:1$ solution of HMDS and acetone for at least 24 hours. After second a fast cleaning (few seconds) with acetone and isopropanol, graphene is deposited onto the wafer by mechanical exfoliation, identified with optical microscopy and characterized by MicroRaman

spectroscopy. In this way, a monolayer graphene flake is chosen and standard ohmic contacts (Ti/Au) are deposited after an electron beam lithography (EBL). For the definition of the constriction/ribbon, a second step of EBL was necessary to define a PMMA mask for the etching process with inductively coupled plasma in O_2 and Ar atmosphere. The device is then suitable for transport measurements after a second immersion in HDMS for at least 24 hours.

S5. Raman spectra and electron mobility in HMDS treated graphene samples

The treatment with HMDS permits an isolation of the monolayer graphene from the substrate and, consequently, improved mobility and reduced doping effects of the substrate is achieved.[8] The presence of the HMDS polymer is firstly checked by MicroRaman spectroscopy. In Figure S5 we present the normalized Raman spectra of two flakes of graphene.

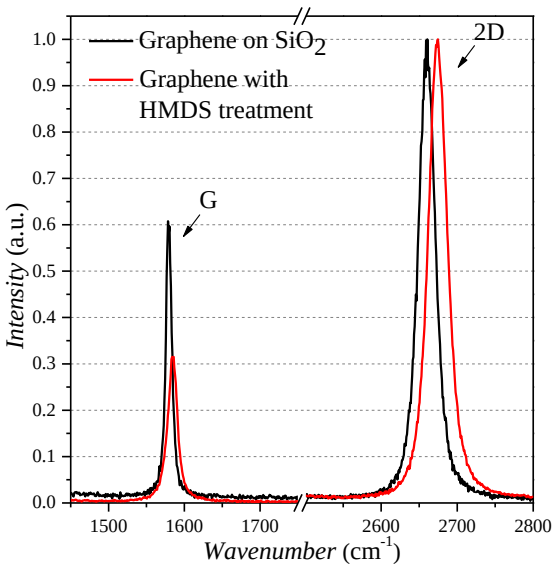

Figure S5: Normalized Raman spectra for graphene on silicon oxide (black line) and graphene with the HMDS treatment (red line).

The black line shows the Raman spectra of a monolayer graphene on Si/SiO_2 substrate and the red line corresponds to a monolayer graphene on Si/SiO_2 substrate with HMDS treatment. The intensity is normalized to the unit to clearly see the difference in the ratio between the 2D-peak and the G-peak, the shifts between G and 2D peak depend on the doping level.[9] The enhancement of the ratio with the HMDS treatment (larger than a factor 3) is an indication of the improvement of the quality of the sample.[10]

Using Equation (2) we estimated the mobility in the range $13\,000 - 20\,000\,\mathrm{cm^2\,V^{-1}\,s^{-1}}$ at 4 K in graphene flakes with HMDS treatment. With these values, the mean free path is found to be smaller than 200 nm.

S6. Measurements on a GNC with HMDS treatment

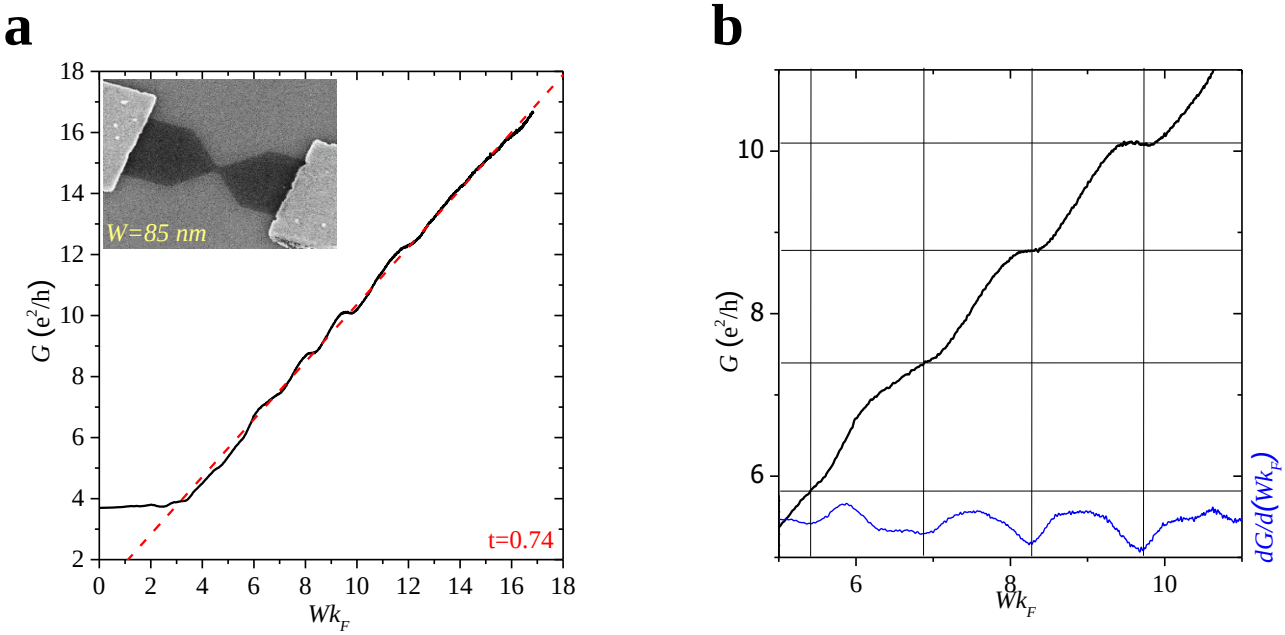

Figure S6: (a) Conductance versus Wk_F of a NC of 85 nm with HMDS treatment. (b) Enlarged view of the conductance (black line) and transconductance (blue line) versus Wk_F.

Due to the lower mean free path in these samples with respect to the encapsulated GNC, we study a GNC of 85 nm on a monolayer graphene flake with HMDS treatment. In

Figure S6(a) we present the conductance in units of e^2/h as a function of Wk_F.

From the linear fit (dashed red line) of the conductance versus Wk_F we found a transmission parameter $t = 0.74$ for the GNC in HMDS. The quality of the edges of the GNC are very good as shown in the insert of the Figure S6(a), where a SEM image of the same structure is shown. It is most important to highlight that the etching process of a sub-nm monolayer graphene is rather less complex than encapsulated graphene, due to the dielectric nature and thickness of hBN. The main limitation of the HMDS GNCs is the small mean free path, that ensure the real ballistic regime only in small constrictions but not on the whole device. The smaller value of t in our HMDS-NC and others[11] could be related to the much lower mobility achieved. In Figure S6b we plot the conductance (black line) and the transconductance (blue line) versus Wk_F. A sequence of three quantized plateaus appear with a separation less than $2e^2/h$.

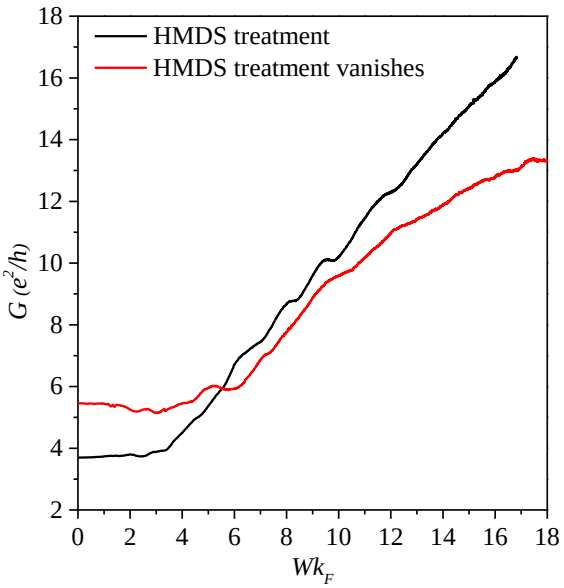

Figure S7: Conductance in units of e^2/h versus Wk_F of a HMDS GNC (black line) and without HMDS (red line).

The effect of HMDS disappears after 2 days in air and less than two weeks in high vacuum at cryotemperatures. In Figure S7, the black line shows the conductance as a function of

Wk_F of the GNC ($W = 85\,\mathrm{nm}$) with HMDS treatment, while the red line is the conductance of the same GNC after the HMDS effect disappeared.

References

(1) Purdie, D.; Pugno, N.; Taniguchi, T.; Watanabe, K.; Ferrari, A.; Lombardo, A. *Nat.Comm.* **2018**, *9*, 5387.

(2) Ferrari, A. C.; Meyer, J. C.; Scardaci, V.; Casiraghi, C.; Lazzeri, M.; Mauri, F.; Piscanec, S.; Jiang, D.; Novoselov, K. S.; Roth, S.; Geim, A. K. *Phys.Rev.Lett.* **2006**, *97*, 187401.

(3) Berciaud, S.; Ryu, S.; Brus, L. E.; Heinz, T. F. *Nano Lett.* **2006**, *9*, 346.

(4) Pizzocchero, F.; Gammelgaard, L.; Jessen, B. S.; Caridad, J. M.; Wang, L.; Hone, J.; Bøggild, P.; Booth, T. J. *Nat. Comm.* **2016**, *7*, 11894.

(5) Neumann, C.; Reichardt, S.; Venezuela, P.; Drøgeler, M.; Banszerus, L.; Schmitz, M.; Watanabe, K.; Taniguchi, T.; Mauri, F.; Beschoten, B.; Rotkin, S.; Stampfer, C. *Nat. Comm.* **2015**, *6*, 8429.

(6) Kim, S.; Nah, J.; Jo, I.; Shahrjerdi, D.; Colombo, L.; Yao, Z.; Tutuc, E.; Banerjee, S. K. *Appl. Phys. Lett.* **2009**, *94*, 062107.

(7) Terrés, B.; Chizova, L. A.; Libisch, F.; Peiro, J.; Jörger, D.; Engels, S.; Girschik, A.; Watanabe, K.; Taniguchi, T.; Rotkin, S. V.; Burgdörfer, J.; Stampfer, C. *Nat. Commun.* **2016**, *7*, 11528.

(8) Lafkioti, M.; Krauss, B.; Lohmann, T.; Schieschang, U.; Klauk, H.; v. Klitzing, K.; Smet, J. H. *Nano Lett.* **2010**, *10*, 1149.

(9) Das, A.; Pisana, S.; Chakraborty, B.; Piscanec, S.; Saha, S. K.; Waghmare, U. V.; Novoselov, K. S.; Krishnamurthy, H. R.; Geim, A. K.; Ferrari, A. C.; Sood, A. K. *Nat.Nanotech.* **2008**, *3*, 210.

(10) Min, B.; Kim, S.; Kim, S.; Kang, M.; Noothongkaew, S.; Mills, E.; Song, W.; Myung, S.; Lim, J.; Kim, S.; An, K.-S. *ACS Appl. Mater. Interfaces* **2016**, *8*, 27421.

(11) Caridad, J. M.; Power, S. R.; Lotz, M. R.; Shylau, A. A.; Thomsen, J. D.; Gammelgaard, L.; Booth, T. J.; Jauho, A.-P.; Bøggild, P. *Nat. Commun.* **2018**, *9*, 659.